

Network of off-axis melt bodies at the East Pacific Rise

J. P. Canales^{1*}, H. Carton², S. M. Carbotte², J. C. Mutter², M. R. Nedimović^{2,3}, M. Xu⁴, O. Aghaei³, M. Marjanović² and K. Newman²

Magmatic accretion of new oceanic crust at intermediate- to fast-spreading mid-ocean ridges occurs along a narrow axial zone. This zone is characterized by molten sills in the crust that are emplaced within about 3 km of the ridge axis¹ and overlie a zone of elevated temperatures and partial melt^{2–4}. There are disparate indications of off-axis magmatism^{5–8} and lavas erupted in the near-axis region are more compositionally variable than in the axial zone⁹. Here we present three-dimensional seismic reflection images from the fast-spreading East Pacific Rise that reveal a network of sills 4 to 8 km east of the ridge axis. Our crustal model, constrained using seismic velocity and attenuation data, shows that the sills are located outside of the main axial zone of crustal accretion, and above a region containing partial melt. We infer that the sills represent sites of sustained off-axis magmatism. Pockets of melt extend from the off-axis sills to the axial zone and may represent melt migration pathways. These pathways could promote mixing between enriched off-axis melts and normal on-axis melts, contributing to the compositional variability of the near-axis lavas⁹. We suggest that off-axis magmatism occurs preferentially, but not exclusively, where pre-existing fractures inherited from offsets of the spreading axis promote melt transport from the mantle into the crust.

The East Pacific Rise (EPR) between 9° and 10° N is the most extensively studied section of the global ridge system¹⁰. Here the Cocos and Pacific tectonic plates spread apart at a full rate of 112 mm yr⁻¹ (ref. 11), forming oceanic crust with an average thickness of 6.8 km (ref. 12). North of 9° 20' N, a 0.25–1.2-km-wide¹³, 30-m-thick¹⁴ crustal melt sill is present beneath the spreading axis at 1.4–1.9 km depth^{1,13}. Between ~9° 46' N–9° 51' N, the ridge crest hosts abundant high-temperature hydrothermal vents¹⁰ and it is the most volcanically active portion of this ridge section, having experienced two well-documented eruptions in 1991–1992 (ref. 15) and 2005–2006 (ref. 16; Fig. 1).

To understand the fine-scale relationships between the crustal magmatic system and the volcanic, tectonic and hydrothermal features of the sea floor we conducted a three-dimensional (3D) multichannel seismic survey of the EPR between 9° 35.6' N and 9° 57.0' N (cruise MGL0812, Fig. 1). The experimental configuration¹⁷ resulted in a dense set of common-mid-point seismic reflection profiles (that is, in-lines), separated 37.5 m from each other and oriented orthogonal to the ridge axis, that allows full 3D processing (Methods). Within survey areas where 3D coverage was complete (that is, within 10 km of the ridge axis between 9° 37.6' N and 9° 39.8' N and between 9° 41.7' N and 9° 57.0' N, Fig. 1), unambiguous recognition of a series of off-axis intra-crustal

reflections was possible because of the high spatial density of the data. Here we report observations from a seismic volume obtained after 3D processing of a sub-set of the data covering the ridge crest between 9° 50' N and 9° 57' N and its eastern flank, where the most prominent and largest concentration of off-axis reflections were identified (Fig. 1).

Visualization of the seismic volume shows that the reflection from the top of the axial magma chamber (AMC) is present along the full length of the study area (Fig. 2a) at a depth of 1.4 km below the sea floor (bsf; Fig. 3a). The AMC is marked by a zone of strong reflection energy that is wider south of 9° 51.5' N, coincident with the 2005–2006 fissure eruptions emanating from the axial summit trough¹⁶ (AST; Fig. 2a), and narrower between 9° 52' N and 9° 56' N (Fig. 2a). Along this ridge section no strong AMC reflections are detected directly beneath the seafloor extent of the 2005–2006 eruption, which occurred along a fissured, ridge-parallel mound ~600 m east of the axis¹⁶ (Fig. 2a).

Within this volume we observe three major intra-crustal reflections 4–8 km to the east of the ridge axis (Fig. 2a). The similarity between the AMC and off-axis reflections and their reversed polarity when compared with seafloor and crust–mantle boundary (Moho) reflections (Fig. 3) indicate that these events arise from negative impedance contrasts. Furthermore, data from the 1997 UNDERSHOOT seismic refraction experiment¹⁸ provide independent evidence that the off-axis events are associated with elevated temperatures and the presence of partial melt within the lower crust. Seismograms of shots located over and immediately to the south of the off-axis events recorded by instruments deployed northeast and east of the study area (Fig. 4a and Supplementary Fig. S6) allow comparison of the amplitudes of seismic waves that travelled through the off-axis events with those from nearby shots. These seismograms show that seismic waves propagating through the off-axis event region were more attenuated than waves propagating outside of this region (for example, by a factor of ~7 for source–receiver offsets of 20 km; Fig. 4b,c; Supplementary Fig. S6). This attenuation effect is local and restricted to the off-axis event region; data from other instruments located further south and on the west flank of the ridge do not show this kind of off-axis attenuation pattern (Supplementary Fig. S6). The observed attenuation pattern indicates the presence of an attenuating low-velocity zone (LVZ) beneath the off-axis events that is at least 2 km thick (Supplementary Figs S7, S8). Therefore, on the basis of the reversed polarity of the off-axis events and the attenuating character of the crust beneath them, we interpret the off-axis seismic events as partially molten crustal sills (hereinafter referred to as off-axis melt lenses, OAMLs).

¹Department of Geology and Geophysics, Woods Hole Oceanographic Institution, Woods Hole, Massachusetts 02540, USA, ²Lamont-Doherty Earth Observatory, Columbia University, Palisades, New York 10964, USA, ³Department of Earth Sciences, Dalhousie University, Halifax, Nova Scotia B3H4J1, Canada, ⁴Massachusetts Institute of Technology-Woods Hole Oceanographic Institution Joint Program in Oceanography, Department of Geology and Geophysics, Woods Hole Oceanographic Institution, Woods Hole, Massachusetts 02540, USA. *e-mail: jpcanales@whoi.edu.

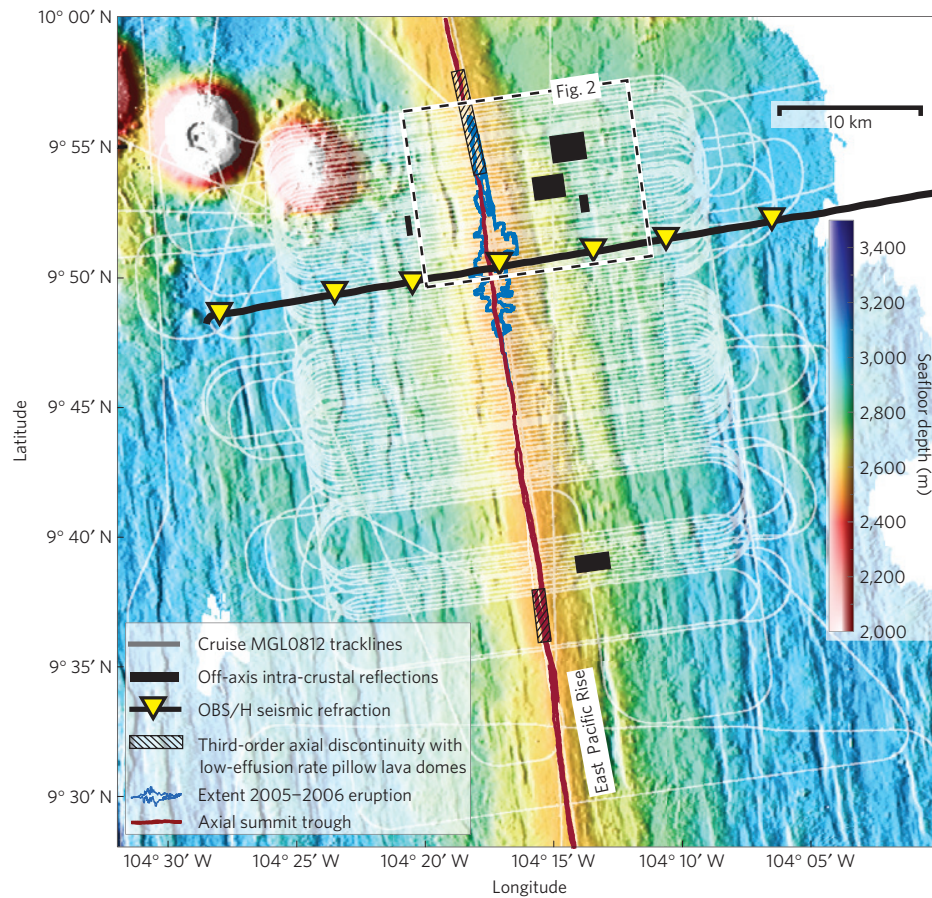


Figure 1 | Bathymetry of the East Pacific Rise and its flanks between 9° 28' N and 10° 00' N latitude from cruise MGL0812. Solid box represents the extent of the seismic volume analysed for this study. Black line corresponds to an ocean-bottom seismometer/hydrophone (OBS/H) seismic refraction profile acquired during the 1997 UNDERSHOOT experiment¹⁸. Locations of pillow lava domes are from ref. 26.

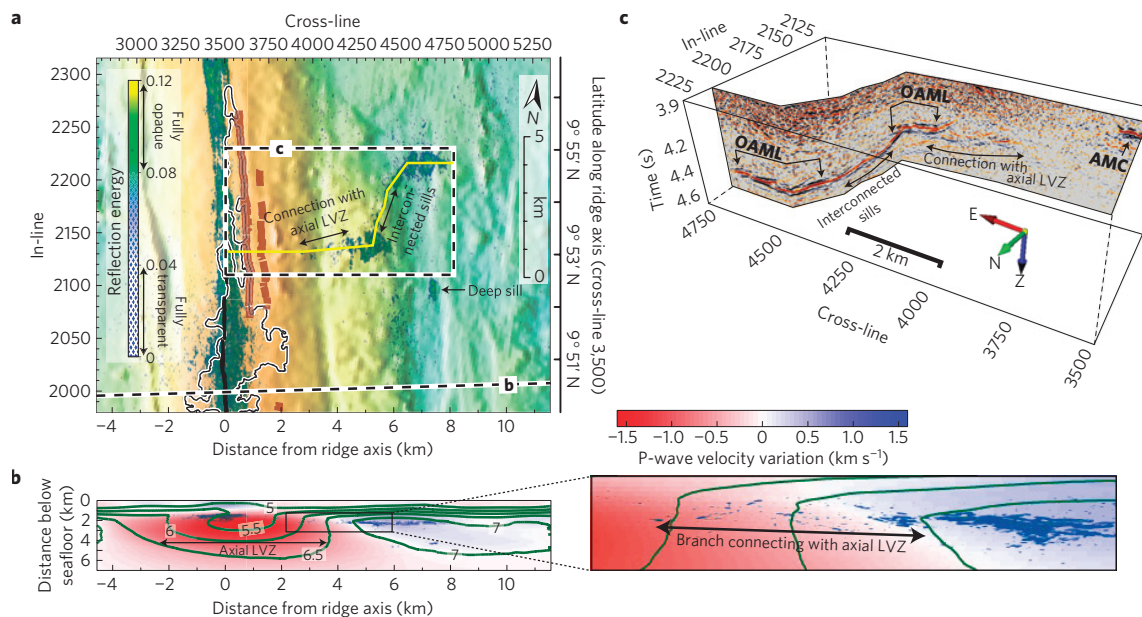


Figure 2 | Seismic reflection energy and vertical sections through the off-axis network. **a**, Reflection energy (Methods) projected onto bathymetry (colour scale as in Fig. 1). Bold and thin black contours in **a** delineate the AST and the extent of the 2005–2006 eruption, respectively. Brown lines are inward-dipping normal faults¹⁶. **b**, Tomography model (Methods) along seismic profile (Fig. 1) with reflection energy projected on cross-section. Iso-velocity contours (green) are labelled in km s^{-1} . Colours represent seismic velocity variations relative to the off-axis average (>3 km from axis). **c**, Fence diagram of vertical seismic reflection sections through the OAML region (path shown as yellow lines in **a**).

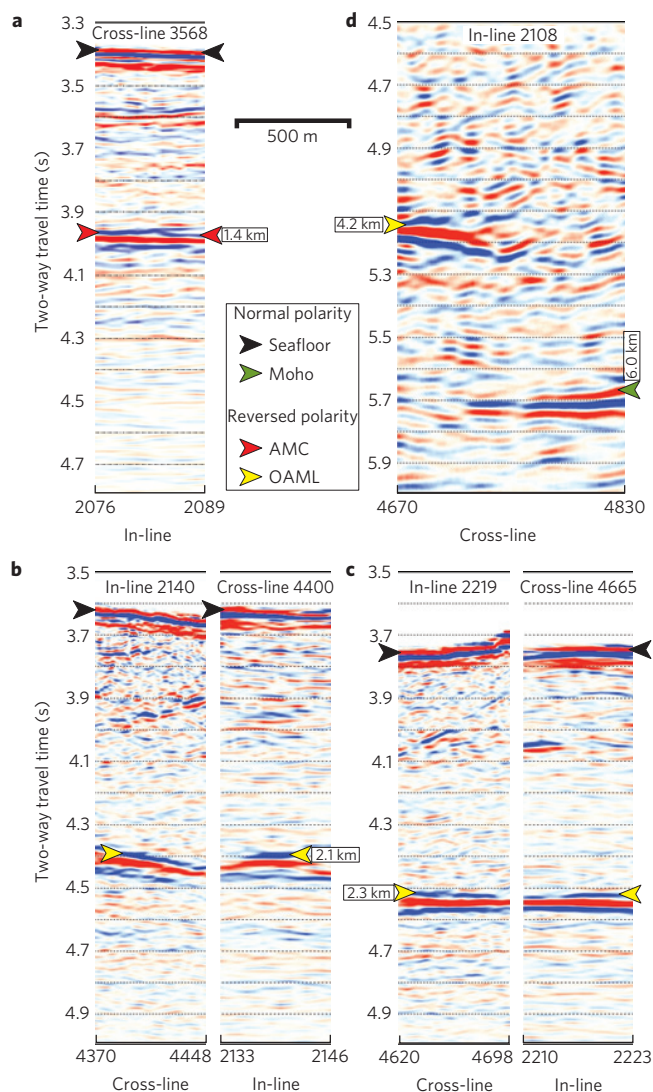


Figure 3 | Seismic sections illustrating the polarity of the main reflections. Reflectors associated with positive impedance contrasts such as the sea floor and the Moho show normal polarity (red-blue-red), whereas the reversed polarity (blue-red-blue) of the AMC and OAML reflections indicates a decrease in acoustic impedance. Labels indicate depth below the sea floor in km. **a**, AMC; **b**, mid-crustal OAML 5.5 km off axis; **c**, mid-crustal OAML 7 km off axis; **d**, lower-crustal OAML 7.5 km off axis (low-pass filtered 15–30 Hz to enhance Moho reflection).

The most distinct features are two mid-crustal OAMLs (1.5×1 and 2×1 km²) found 5.5 km and 7 km east of the rise axis at depths of 2.1 and 2.3 km bsf, respectively (Figs 2, 3b,c). These OAMLs are 2.5 km apart from each other, forming a network of sills inter-connected by a narrow channel of melt pockets (Fig. 2a,c). A smaller OAML (530×170 m²) is present 7.5 km east of the axis within the lower crust at a depth of 4.2 km bsf (Figs 2a, 3d).

Compressional seismic velocities were determined along a seismic refraction profile from the UNDERSHOOT experiment crossing the ridge crest at 9° 50.4' N, roughly coincident with in-line 2003 (Figs 1, 2a). The tomography velocity model (Methods) shows a 6-km-wide LVZ underlying the AMC reflection (Fig. 2b and Supplementary Fig. S5). If the velocity structure along this cross-section is also representative of the crustal structure across the OAML region a few kilometres to the north, then the OAMLs are located outside of the axial accretionary zone in a region of normal-to-high velocities, suggesting a fully solidified crust

(Fig. 2b). Assuming that at 4–8 km off-axis the crustal temperature at 2 km depth is 250 °C (ref. 2), a 30–100-m-thick sill^{14,19} would conductively solidify in 7–75 years (Methods). Heat removal by hydrothermal circulation would decrease the solidification time by a factor of 8–12 (ref. 20). This solidification time is less than the minimum age (11 years) required for the OAMLs to have been detected in the 1997 UNDERSHOOT dataset (Fig. 4), therefore indicating that the OAMLs are somewhat thicker (>100 m) than AMC estimates^{14,19}, that hydrothermal cooling in this area is less efficient than estimated from numerical models²⁰, or that the OAML region is a site of sustained crustal magmatism with frequent replenishment of the OAMLs. We favour the latter hypothesis on the basis of the seismic attenuation observed in the UNDERSHOOT data (Fig. 4), which indicates elevated temperatures and partial melt within a lower crustal volume at least 2 km thick (Supplementary Figs S7,S8).

The vast majority of lavas sampled along the AST of the EPR are normal mid-ocean ridge basalts (N-MORBs) with homogeneous compositions, whereas lavas sampled outside of the AST up to ~4 km off-axis exhibit a much wider range of compositions, including enriched (E-) MORBs (ref. 9). The prevalence of E-MORBs in off-axis samples has been attributed to off-axis eruptions fed by small magma bodies separated from the axial magma system that tap mantle melts generated away from the main melt zone⁹, a model supported by the young age of some off-axis lavas⁸. Alternatively, the prevalence of E-MORBs in off-axis samples and their apparent young age could be due to lavas erupted on-axis that flowed down the ridge flanks²¹. Our finding of OAMLs 4–8 km off-axis strongly supports the model of off-axis magma bodies⁹. In our study area, numerous off-axis lava samples have enriched compositions²¹ (Supplementary Fig. S9), and the majority of off-axis samples between 9° 49' N and 9° 52' N that have been analysed for U-series disequilibria have radiogenic ages younger than predicted by the spreading rate²¹. Thus, it is reasonable to hypothesize that eruptions from the OAMLs contribute to E-MORBs in off-axis lavas, although no samples have been collected from sea floor directly above these features (Supplementary Fig. S9).

Our high-resolution seismic volume also reveals a channel of reflectivity that branches out from the large sill closer to the ridge axis, extending sub-horizontally up to the eastern side of the ridge crest (Fig. 2a–c). This channel does not intersect the AMC but extends into the axial LVZ, indicating that the imaged off- and on-axis magmatic systems are connected to each other (Fig. 2c). Whether the axial magmatic system feeds melts to the OAMLs or vice versa remains unconstrained. However, buoyancy arguments favour an uphill path for melts, from the deeper network of OAMLs towards the shallower top of the axial LVZ. Enriched magmas from the OAMLs entrained into the axial accretionary zone could then mix with the axial magmas and contribute to variable extents of mixing between enriched and depleted compositions in the near-axis region, as documented in the 9° 31' N section of the EPR (ref. 9).

Numerical simulations predict that melts extracted from the mantle accumulate at a permeability barrier developed at the base of a sloping thermal boundary layer, extending many tens of kilometres away from the ridge axis²², as supported by some observations⁶. The majority of melt will be focused laterally towards the spreading axis²², but vertical delivery of melt from this magma reservoir into the overlying crust may also occur locally where the permeability barrier is absent or weakly developed because of compositional or thermal heterogeneities⁵ and/or intense faulting and fracturing. Axial discontinuities are known to be associated with sheared and/or fractured crust, in many cases producing morphological and geophysical anomalies across the ridge flanks^{11,12}. The off-axis remnants of axial discontinuities may persist as zones of crustal weakness on the ridge flanks²³, and thus are strong candidates where off-axis magmatism may

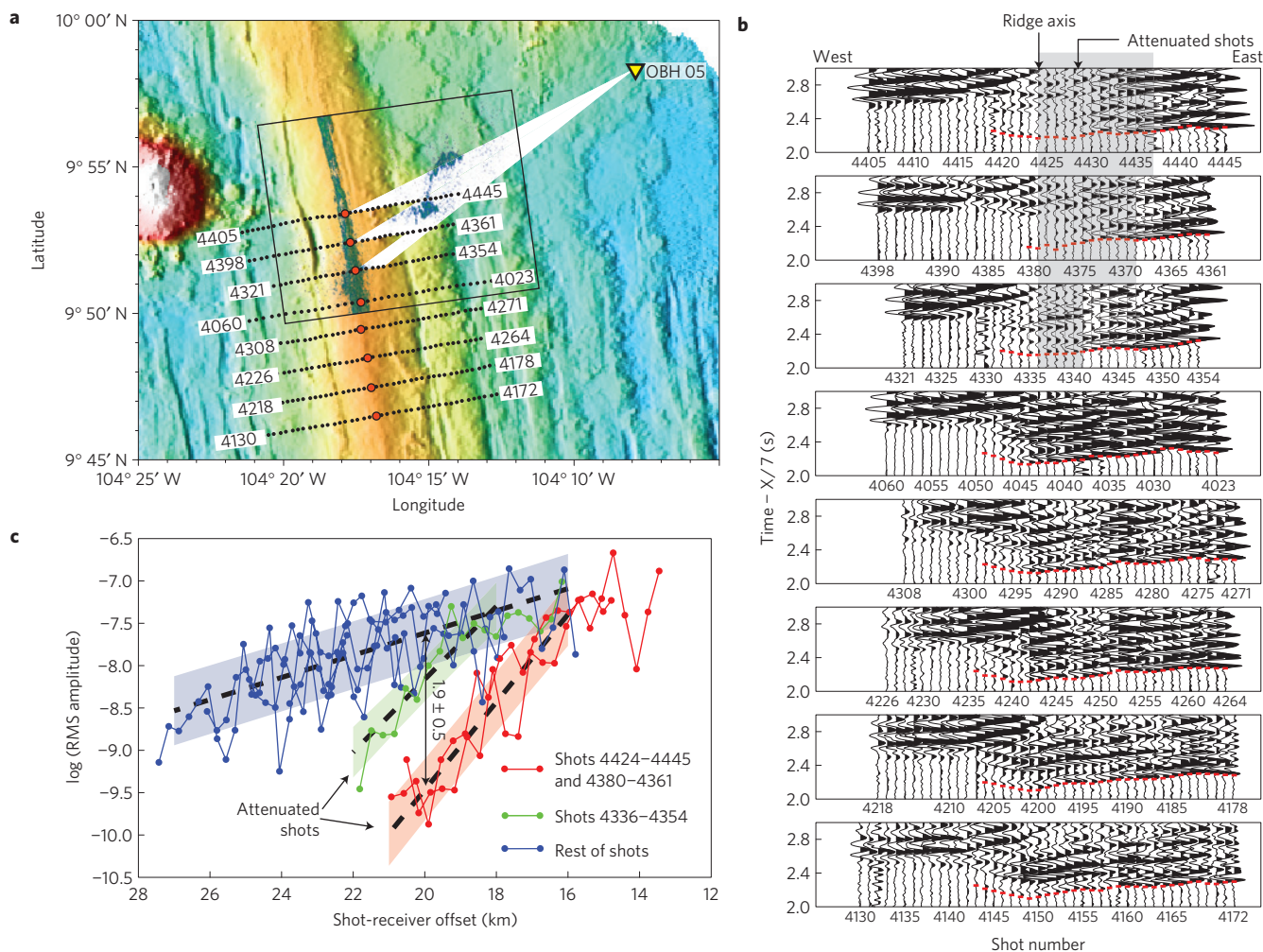


Figure 4 | Wide-angle seismic data showing attenuation in the OAML region. a, Bathymetry with projected seismic reflection energy. Black dots are shot locations from the UNDERSHOOT experiment (labelled at the eastern and western ends of shooting lines). **b**, Seismic traces from UNDERSHOOT OBH 05 (location in **a**) displayed with constant scaling for shots shown in **a** (panels top-to-bottom arranged from north to south). **c**, Natural log of RMS amplitude (within a 150-ms-window from the first arrival, red ticks in **b**) for shots east of the ridge axis (red circles in **a**). Dashed lines are linear fits to data points with offsets >16 km (blue and red) and >18 km (green). Shading shows $\pm 1\sigma$ of the fit. At 20 km offset, data from the two northern lines have 1.9 ± 0.5 log units less RMS amplitude than data from the other lines (decrease in amplitude by a factor of ~ 7). Shots with anomalous amplitude are highlighted in **b** (grey background) and **a** (white ray-path swaths).

preferentially—but not exclusively—occur, perhaps aided by plate-bending stresses²⁴. Supporting this hypothesis is our finding that the two regions with OAMLs within less than 10 km of the ridge axis are both near third-order axial discontinuities (Fig. 1). Our survey detected an OAML immediately north of a discontinuity at $9^{\circ} 37' \text{ N}$ (ref. 25), and the $9^{\circ} 54' \text{ N}$ OAML region is located east of an axial discontinuity zone²⁶: between $9^{\circ} 51.5' \text{ N}$ and $9^{\circ} 54' \text{ N}$ the ridge crest shows counter-clockwise rotation²⁶, the AMC narrows (Fig. 2a) and the axial depth increases abruptly²⁷, the AST—a feature related to dike injection and high-effusion rate volcanic activity²⁷—becomes discontinuous and eventually disappears²⁷ (Fig. 2a), and seafloor volcanism transitions from high- to low-effusion rate eruptions²⁶.

Along the EPR between $9^{\circ} 09' \text{ N}$ and $10^{\circ} 00' \text{ N}$, axial pillow lava domes indicative of low-effusion rate eruptions (primarily attributed to narrow conduits and/or low magma driving pressure²⁶) are rare but consistently present at all of the third-order axial discontinuities found along this ridge segment²⁶. Our finding that OAMLs located less than 10 km from the ridge axis are spatially correlated with these zones indicates that off-axis magmatism may influence the eruptive style at the ridge crest. Tapping of melts by the off-axis system could reduce the availability of melt for

the axial region, resulting in lower magma pressures at the ridge axis. Furthermore, lower magmatic pressure within the AMC could make eruptions more sensitive to local stress field variations. For example, during the 2005–2006 eruption, lavas north of $9^{\circ} 53' \text{ N}$ erupted $\sim 600 \text{ m}$ east of the spreading axis instead of directly above the AMC (Fig. 2a). It has been suggested²⁸ that this misalignment between the seafloor eruption and the ridge axis could have been promoted by the fault(s) bounding the eruption to the east between $9^{\circ} 53' \text{ N}$ and $9^{\circ} 56' \text{ N}$ (Fig. 2a). A local stress perturbation imposed by these faults²⁸ could have deflected the feeding dike away from the AMC if magmatic pressure during the eruption was insufficient to drive dikes straight up to the sea floor. Thus we argue that the characteristics of the 2005–2006 eruption between $9^{\circ} 53' \text{ N}$ and $9^{\circ} 56' \text{ N}$, the transition in eruptive style within this region, and the presence of OAMLs can be explained by partitioning in magma supply between the axial and off-axis magmatic systems.

Methods

Seismic reflection data processing. A summary of acquisition parameters is given in Supplementary Table S1 (full details are available in ref. 17) and processing steps in Supplementary Table S2.

Seismic reflection data visualization. To facilitate visualization of the reflectivity of the AMC and OAML events (Fig. 2a) we applied a top mute to the seismic volume to suppress high-amplitude events within upper crust, such as sea floor, base of layer 2A and shallow faults. This top mute was carefully hand-picked to ensure that none of the AMC and OAML events were masked out. Supplementary Fig. S2 shows an example of the mute designed for in-line 2210.

The reflectivity of the seismic volume shown in Fig. 2a corresponds to the energy attribute of each seismic trace averaged within a sliding 16-ms gate (that is, the squared sum of the sample values within the specified gate divided by the number of samples in the gate), visualized with a colour palette transparent at the low end of the scale.

Sill solidification time. The sill solidification time t_s is $t_s = b^2/4\kappa\lambda_2^2$ (ref. 29), where b is the half-thickness of the sill, κ is the thermal diffusivity ($6.3 \times 10^{-7} \text{ m}^2 \text{ s}^{-1}$) and λ_2 is obtained from $L\sqrt{\pi}/c(T_m - T_0) = e^{-\lambda_2^2}/\lambda_2(1 + \text{erf } \lambda_2)$. L is latent heat ($4 \times 10^5 \text{ J kg}^{-1}$), c is specific heat ($1.2 \times 10^3 \text{ J kg}^{-1} \text{ K}^{-1}$), T_m is the liquid magma temperature (1,200 °C) and T_0 is the temperature of the host rock (250 °C).

Seismic refraction data and modelling. During the 1997 UNDERSHOOT experiment¹⁸ wide-angle seismic refraction data were collected along a ridge-perpendicular profile crossing the EPR crest near 9° 50' N, roughly coincident with our in-line 2003 (Fig. 1). Seven ocean bottom seismometers (OBS) and hydrophones (OBH; Fig. 1) recorded energy generated by air-gun shots triggered every ~450 m along the profile. To obtain a P-wave crustal velocity model across this part of the EPR we conducted a tomographic inversion of travel times of crustal refractions (P_g) and Moho reflections (P_mP ; Supplementary Fig. S3).

To solve for the crustal seismic velocity field and the depth to the Moho we applied a joint refraction–reflection travel-time tomography method³⁰, a nonlinear inversion regularized by imposing damping and smoothing constraints. To minimize possible biases in the inversion result due to the choice of starting model, we followed a Monte Carlo approach and conducted a large number (100) of tomographic inversions, starting with different, randomized 1D models (Supplementary Fig. S4; ref. 30). Starting models produce a RMS misfit between observed and predicted travel times ranging between 97 and 373 ms. The preferred velocity model was then taken as the mean of the 100 Monte Carlo solutions (Supplementary Fig. S5). This model reduces the travel-time misfit to 19 ms. The velocity model was used to convert the two-way travel time of the reflections discussed in the paper to depth (Fig. 3).

Received 31 December 2010; accepted 22 December 2011;
published online 29 January 2012

References

- Detrick, R. S. *et al.* Multi-channel seismic imaging of a crustal magma chamber along the East Pacific Rise. *Nature* **326**, 35–41 (1987).
- Dunn, R. A., Toomey, D. R. & Solomon, S. C. Three-dimensional seismic structure and physical properties of the crust and shallow mantle beneath the East Pacific Rise at 9° 30' N. *J. Geophys. Res.* **105**, 23537–23555 (2000).
- Wilcock, W. S. D., Solomon, S. C., Purdy, G. M. & Toomey, D. R. The seismic attenuation structure of a fast-spreading mid-ocean ridge. *Science* **258**, 1470–1474 (1992).
- Crawford, W. C. & Webb, S. C. Variations in the distribution of magma in the lower crust and at the Moho beneath the East Pacific Rise at 9°–10° N. *Earth Planet. Sci. Lett.* **203**, 117–130 (2002).
- Durant, D. T. & Toomey, D. R. Evidence and implications of crustal magmatism on the flanks of the East Pacific Rise. *Earth Planet. Sci. Lett.* **287**, 130–136 (2009).
- Garmany, J. Accumulations of melt at the base of young oceanic crust. *Nature* **340**, 628–632 (1989).
- Haymon, R. M., Macdonald, K. C., Benjamin, S. B. & Ehrhardt, C. J. Manifestations of hydrothermal discharge from young abyssal hills on the fast-spreading East Pacific Rise flank. *Geology* **33**, 153–156 (2005).
- Goldstein, S. J., Perfit, M. R., Batiza, R., Fornari, D. J. & Murrell, M. T. Off-axis volcanism at the East Pacific Rise detected by uranium-series dating of basalts. *Nature* **367**, 157–159 (1994).
- Perfit, M. R. *et al.* Small-scale spatial and temporal variations in mid-ocean ridge crest magmatic processes. *Geology* **22**, 375–379 (1994).
- Haymon, R. M. *et al.* Hydrothermal vent distribution along the East Pacific Rise crest (9° 09'–54' N) and its relationship to magmatic and tectonic processes on fast-spreading mid-ocean ridges. *Earth Planet. Sci. Lett.* **104**, 513–534 (1991).
- Carbotte, S. M. & Macdonald, K. C. East Pacific Rise 8°–10° 30' N: evolution of ridge segment and discontinuities from SeaMARC II and three-dimensional magnetic studies. *J. Geophys. Res.* **97**, 6959–6982 (1992).
- Canales, J. P., Detrick, R. S., Toomey, D. R. & Wilcock, W. S. D. Segment-scale variations in the crustal structure of 150–300 kyr old fast spreading oceanic crust (East Pacific Rise, 8° 15' N–10° 15' N) from wide-angle seismic refraction profiles. *Geophys. J. Int.* **152**, 766–794 (2003).
- Kent, G. M., Harding, A. J. & Orcutt, J. A. Distribution of magma beneath the East Pacific Rise between the Clipperton transform and the 9° 17' N devial from forward modeling of common depth point data. *J. Geophys. Res.* **98**, 13945–13969 (1993).
- Collier, J. S. & Singh, S. C. Detailed structure of the top of the melt body beneath the East Pacific Rise at 9° 40' N from waveform inversion of seismic reflection data. *J. Geophys. Res.* **102**, 20287–20304 (1997).
- Haymon, R. M. *et al.* Volcanic eruption of the mid-ocean ridge along the East Pacific Rise crest at 9° 45'–52' N: Direct submersible observations of seafloor phenomena associated with an eruption event in April, 1991. *Earth Planet. Sci. Lett.* **119**, 85–101 (1993).
- Soule, S. A., Fornari, D. J., Perfit, M. R. & Rubin, K. H. New insights into mid-ocean ridge volcanic processes from the 2005–2006 eruption of the East Pacific Rise, 9° 46' N–9° 56' N. *Geology* **35**, 1079–1082 (2007).
- Mutter, J. C., Carbotte, S., Nedimović, M. R., Canales, J. P. & Carton, H. Seismic imaging in three dimensions on the East Pacific Rise. *Eos Trans. AGU* **90**, 374–375 (2009).
- Toomey, D. R., Jousset, D., Dunn, R. A., Wilcock, W. S. D. & Detrick, R. S. Skew of mantle upwelling beneath the East Pacific Rise governs segmentation. *Nature* **446**, 409–414 (2007).
- Hussenöder, S. A., Collins, J. A., Kent, G. M. & Detrick, R. S. The TERA Group. Seismic analysis of the axial magma chamber reflector along the southern East Pacific Rise from conventional reflection profiling. *J. Geophys. Res.* **101**, 22087–22105 (1996).
- Phipps Morgan, J. & Chen, Y. J. Dependence of ridge-axis morphology on magma supply and spreading rate. *Nature* **364**, 706–708 (1993).
- Waters, C. L., Sims, K. W. W., Perfit, M. R., Blichert-Toft, J. & Blusztajn, J. Perspective on the genesis of E-MORB from chemical and isotopic heterogeneity at 9–10° N East Pacific Rise. *J. Petrol.* **52**, 565–602 (2011).
- Hebert, L. B. & Montesi, L. G. J. Generation of permeability barriers during melt extraction at mid-ocean ridges. *Geochem. Geophys. Geosyst.* **11**, Q12008 (2010).
- Wilcock, W. S. D., Purdy, G. M., Solomon, S. C., DuBois, D. L. & Toomey, D. R. Microearthquakes on and near the East Pacific Rise, 9°–10° N. *Geophys. Res. Lett.* **19**, 2131–2134 (1992).
- Sohn, R. A. & Sims, K. W. W. Bending as a mechanism for triggering off-axis volcanism on the East Pacific Rise. *Geology* **33**, 93–96 (2005).
- Smith, M. C. *et al.* Magmatic processes and segmentation at a fast spreading mid-ocean ridge: Detailed investigation of an axial discontinuity on the East Pacific Rise crest at 9° 37' N. *Geochem. Geophys. Geosyst.* **2**, 1040 (2001).
- White, S. M., Haymon, R. M., Fornari, D. J., Perfit, M. R. & Macdonald, K. C. Correlation between volcanic and tectonic segmentation of fast-spreading ridges: Evidence from volcanic structures and lava flow morphology on the East Pacific Rise at 9°–10° N. *J. Geophys. Res.* **107**, 2173 (2002).
- Soule, S. A., Escartin, J. & Fornari, D. A record of eruption and intrusion at a fast spreading ridge axis: Axial summit trough of the East Pacific Rise 9–10° N. *Geochem. Geophys. Geosyst.* **10**, Q10T07 (2009).
- Goss, A. R. *et al.* Geochemistry of lavas from the 2005–2006 eruption at the East Pacific Rise, 9° 46' N–9° 56' N: Implications for ridge crest plumbing and decadal changes in magma chamber compositions. *Geochem. Geophys. Geosyst.* **11**, Q05T09 (2010).
- Turcotte, D. L. & Schubert, G. *Geodynamics* (Cambridge Univ. Press, 2002).
- Korenaga, J. *et al.* Crustal structure of the southeast Greenland margin from joint refraction and reflection seismic tomography. *J. Geophys. Res.* **105**, 21591–21614 (2000).

Acknowledgements

This research was funded by the US National Science Foundation. We thank the RV *M.G. Langseth's* Captain M. Landow, crew, and technical staff led by R. Steinhaus for their efforts, which made possible the success of cruise MGL0812. We thank S.A. Soule for providing digital information about the AST and 2005–2006 eruption shown in Fig. 1 and 2, and for stimulating discussions during the preparation of this manuscript. We thank D.R. Toomey for his reviews, which improved the manuscript.

Author contributions

J.P.C. Field program co-leader. MCS data processing and visualization. OBS seismic data analysis and tomography modelling. Geological interpretation. Wrote manuscript. H.C. Data acquisition and quality control. Data processing. Contributed to data processing strategy, interpretation and manuscript writing. S.M.C. Program inception and planning leader. Field program co-leader. Geological interpretation. Contributed to manuscript writing. J.C.M. Program inception. Field program leader. Contributed to interpretation and manuscript writing. M.R.N. Field program co-leader. Contributed to data processing strategy, interpretation and manuscript writing. M.X. Data acquisition and quality control. Data processing. O.A. Data acquisition and quality control. Contributed to data processing strategy. M.M. Data acquisition and quality control. K.N. Data acquisition and quality control.

Additional information

The authors declare no competing financial interests. Supplementary information accompanies this paper on www.nature.com/naturegeoscience. Reprints and permissions information is available online at www.nature.com/reprints. Correspondence and requests for materials should be addressed to J.P.C.

Network of off-axis melt bodies at the East Pacific Rise

J. Pablo Canales^{1*}, Helene Carton², Suzanne M. Carbotte², John C. Mutter², Mladen R. Nedimović^{3,2}, Min Xu⁴, Omid Aghaei³, Milena Marjanović² and Kori Newman²

¹ Department of Geology and Geophysics, Woods Hole Oceanographic Institution, Woods Hole, MA 02540, USA.

² Lamont-Doherty Earth Observatory, Columbia University, Palisades, NY 10964, USA.

³ Department of Earth Sciences, Dalhousie University, Halifax, Nova Scotia B3H4J1, Canada.

⁴ Massachusetts Institute of Technology-Woods Hole Oceanographic Institution Joint Program in Oceanography, Department of Geology and Geophysics, Woods Hole Oceanographic Institution, Woods Hole, MA 02540, USA.

* Corresponding author. E-mail: jpcanales@whoi.edu

Format: PDF

Size: 29.4 MB

This file includes:

SUPPLEMENTARY TABLES (1, 2)

SUPPLEMENTARY FIGURES (S1-S9)

Table 1. Main acquisition parameters during cruise MGL0812	
Vessel	<i>RV Marcus G. Langseth</i>
Hydrophone streamers	Number: 4 Spacing: 150 m Length: 6,000 m Number of groups: 468 Group spacing: 12.5 m
Sources	Number: 2 Source separation: 75 m Number of arrays: 2 per source Number of guns: 9 per array Volume: 54 L (3,300 in ³) per source Source interval: alternate every 37.5 m
Recording	Sampling interval: 2 ms Record length: 10,240 ms Format: SEG-D

Table 2. 3D processing sequence

<p>3D geometry definition</p> <p>Binning: 6.25×37.5 m bins</p> <p>Band-pass filtering: 5-7-200-225 Hz</p> <p>Spherical divergence correction</p> <p>Surface-consistent amplitude correction for shot and channel</p> <p>Offset distribution regularization (flexible binning in cross-line direction): 0.5×bin size for offsets ≤1,662 m; 1.5×bin size for offsets ≥4,587 (linear interpolation offsets in between those values) (Fig. S1).</p> <p>Resample to 4 ms and 7-s trace length.</p> <p>Stacking velocity analysis ^a</p> <p>Normal move-out correction</p> <p>Stretch and outer mute (muted offset>2,000 m for the AMC events, offset>2,500 m for OAML events).</p> <p>Stack CMP gathers</p> <p>Bottom mute of primary seafloor multiple</p> <p>Two-pass (in-line and cross-line directions) f-k domain post-stack time migration</p> <p>Top mute above seafloor</p>
<p>^a Processing was oriented towards optimizing imaging of the axial melt lens and a series of off-axis mid-crustal reflectors. Our stacking velocity model does not include a layer for properly stacking the base of seismic layer 2A, which is a wide-angle reflection¹. Thus the 3D seismic volume obtained from this processing should not be used for interpreting/analyzing layer 2A events or their absence.</p> <p>¹ Harding, A. J., Kent, G. M., and Orcutt, J. A., A multichannel seismic investigation of upper crustal structure at 9°N on the East Pacific Rise: Implications for crustal accretion. <i>J. Geophys. Res.</i> 98, 13,925-13,944 (1993).</p>

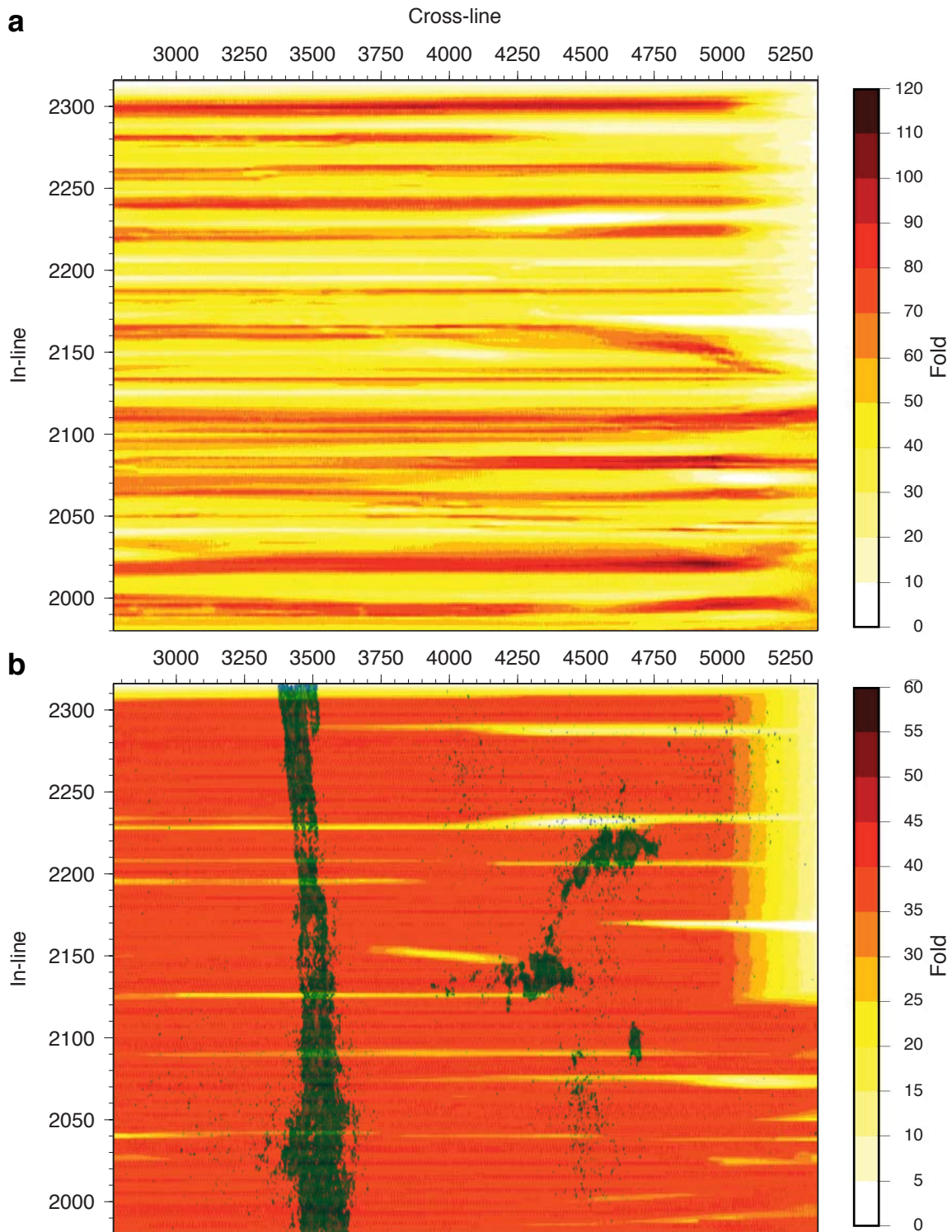


Figure S1. Bin fold maps **a**, before and **b**, after offset distribution regularization. Maximum nominal fold after offset regularization is set to 40. Top-view of the seismic reflectivity of the volume (as in Fig. 2a) has been projected over the fold map.

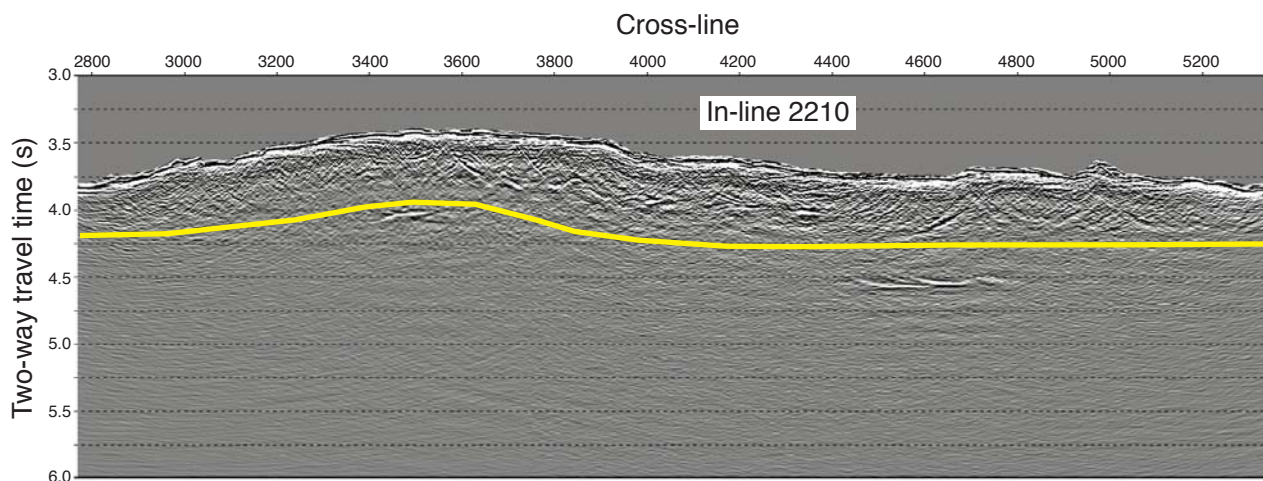


Figure S2. Example of an in-line section showing the top mute (yellow line) applied to the seismic volume prior to calculating the trace energy for 3D visualization of the AMC and OAML events.

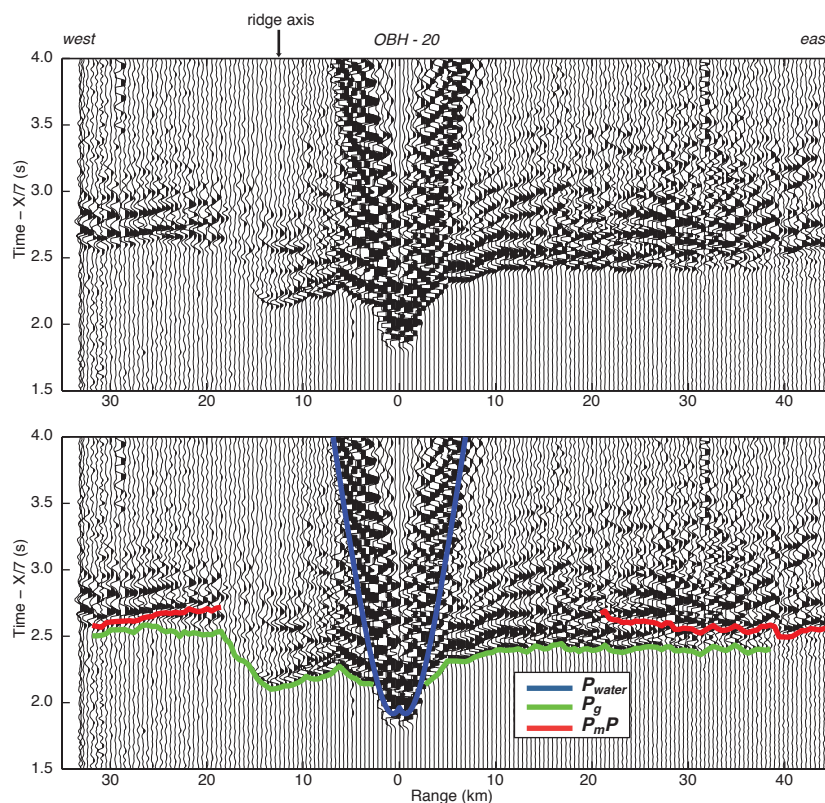


Figure S3. Example of ocean bottom hydrophone record section (top) with main seismic arrivals indicated as colored lines (bottom). Vertical axis is reduced travel time (7 km/s), and horizontal axis is distance between sources and receiver.

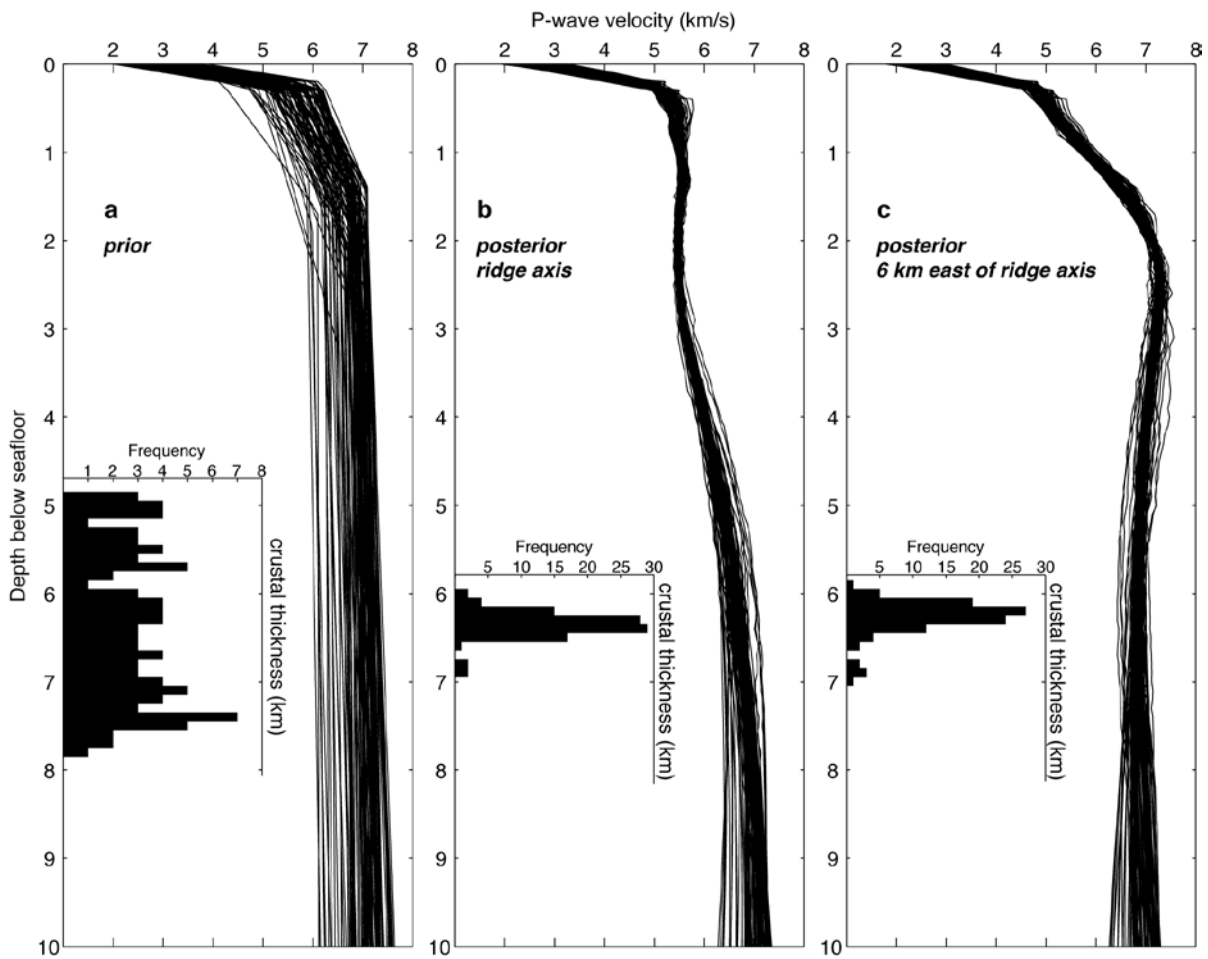


Figure S4. **a**, Prior 100 random Monte Carlo 1D starting models. **b**, Velocity-depth profiles from the 100 Monte Carlo solutions extracted at the location of the ridge axis. **c**, Velocity-depth profiles from the 100 Monte Carlo solutions extracted 6 km to the east of the ridge axis. Insets with vertical histograms show the distribution of prior and posterior crustal thickness models.

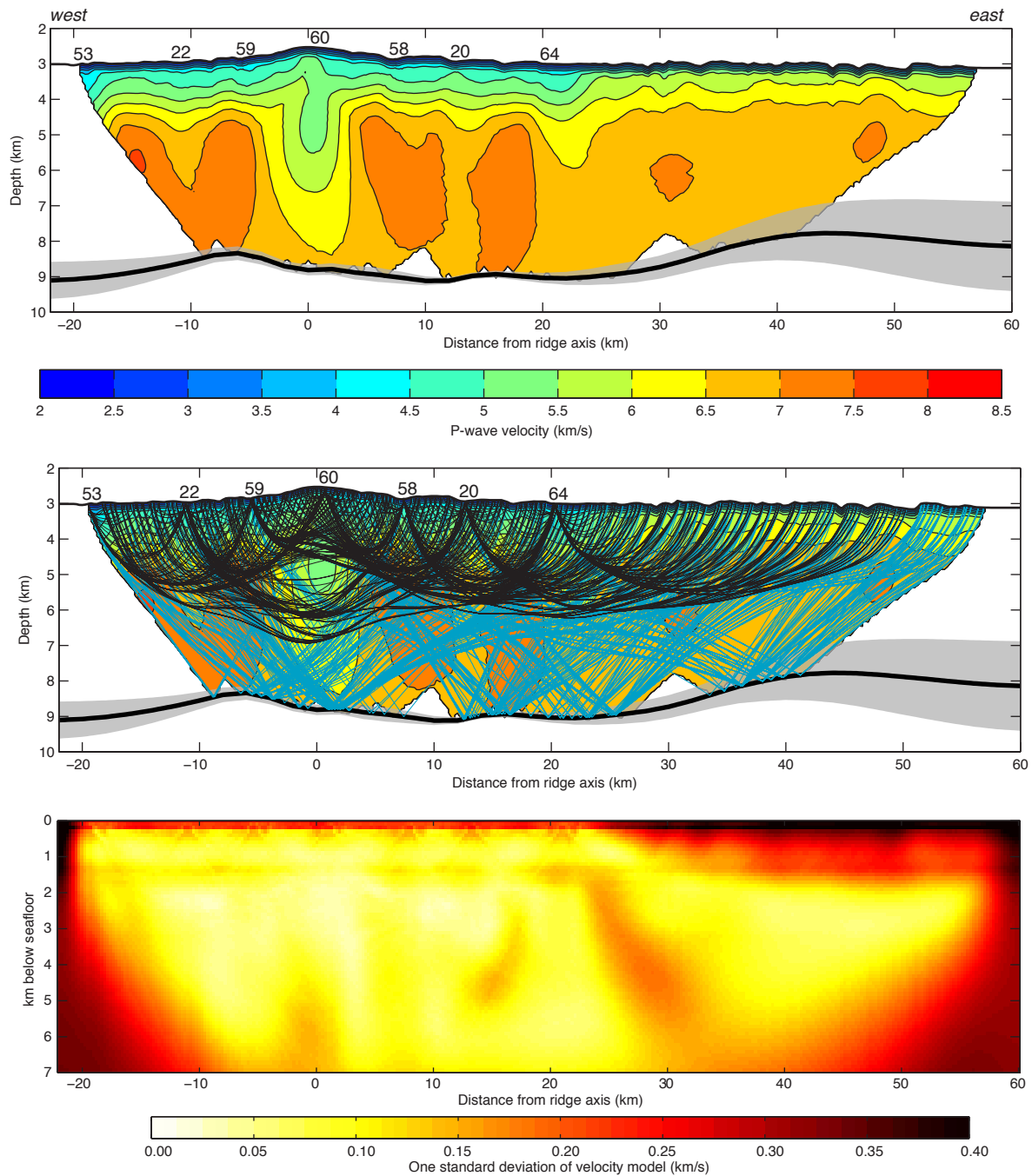


Figure S5. Top: Preferred velocity model (averaged from the 100 Monte Carlo solutions). Only portions of the model constrained by ray paths (middle: black for P_g and blue for P_mP rays) are shown in color. Numbers along bathymetry profile are instrument number. Solid black line is Moho depth (mean of the 100 solutions), and gray bounds show $\pm 1\sigma$. Bottom: One standard deviation map of the 100 Monte Carlo solutions. Note the higher velocity uncertainty in the shallow crust for $X > 20$ km due to lack of recordings along the eastern half of the profile.

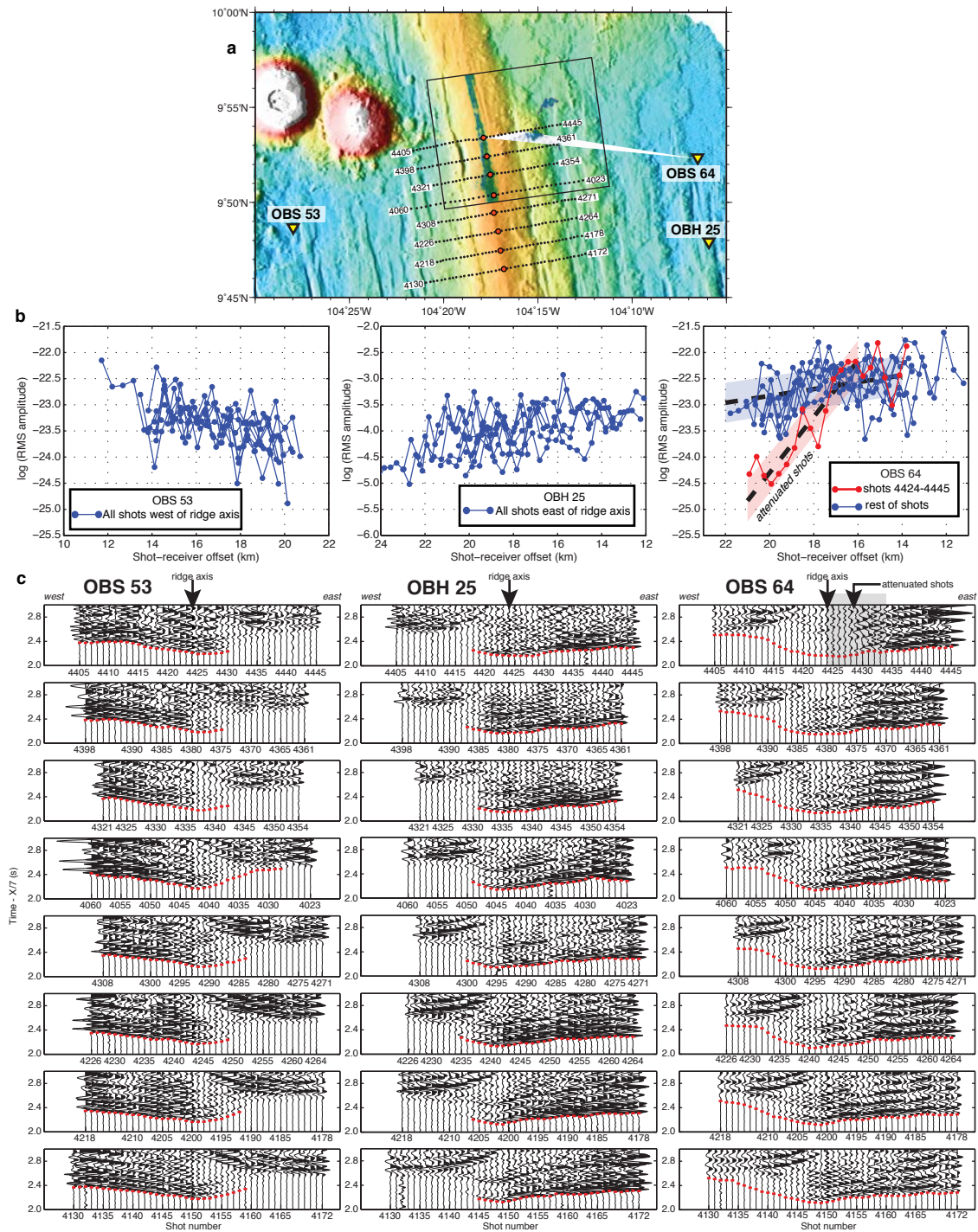


Figure S6. Attenuation analysis of UNDERSHOOT data from instruments OBS 53, OBH 25, and OBS 64. See description of panels and symbols in Fig. 4. Note that, with the exception of shots 4424-4433 recorded by OBS 64, none of the other record sections show evidence of seismic attenuation. This indicates that the attenuation pattern shown in Fig. 4 is a local feature associated with the OAMLs.

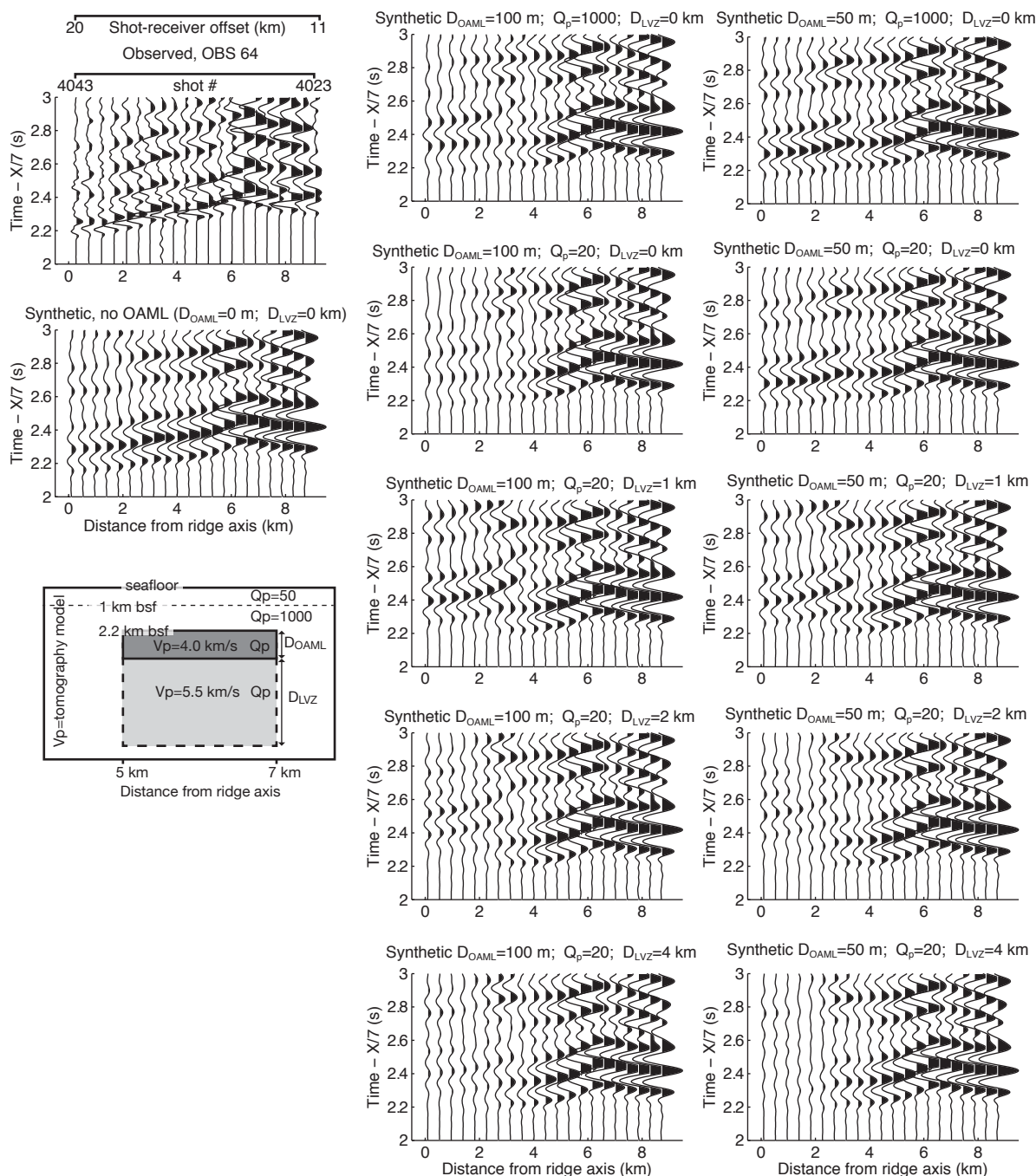


Figure S7. Non-attenuated seismograms from UNDERSHOOT instrument OBS 64 for shots 4023-4043 (Fig. S6) compared to synthetic seismograms calculated for several models with different OAML properties and sub-OAML low velocity volume added to the tomography model of Fig. S5 (diagram). Synthetic seismograms were calculated using a finite-difference approximation of the acoustic wave equation in the frequency domain (Pratt, R. G. & Worthington, M. H. Inverse theory applied to multi-source cross-hole tomography. Part 1: Acoustic wave-equation method. *Geophysical Prospecting* **38**, 287-310 (1990)). Source wavelet is a three-excursion Kupper wavelet with central frequency at 6 Hz, band-pass filtered between 4-5-8-10 Hz to simulate the narrow frequency content of the OBS data. Velocity, density, and attenuation models were discretized at 12.5 m intervals. Synthetic seismograms were calculated for 15 frequency components evenly sampled between 1 and 15 Hz

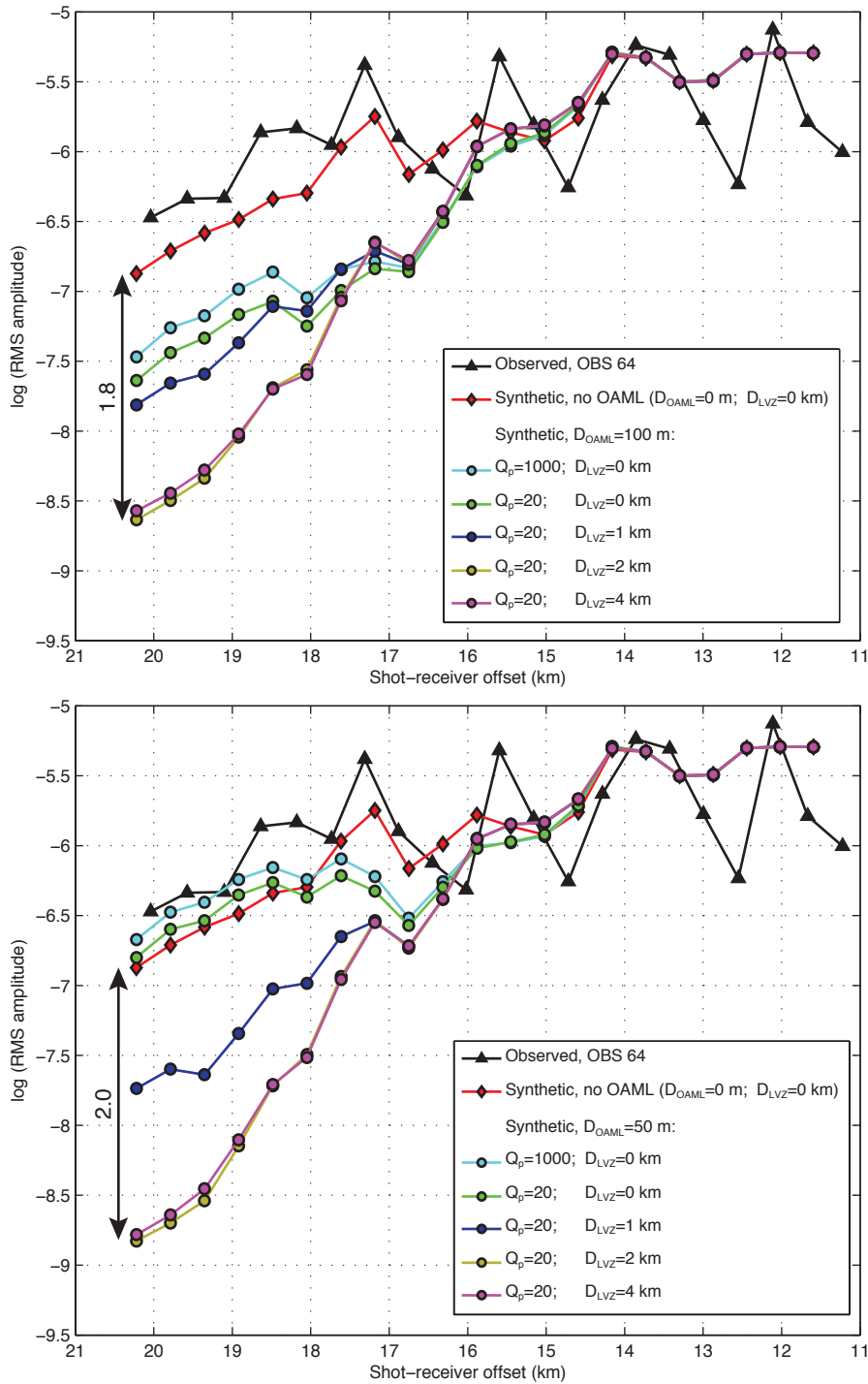


Figure S8. RMS amplitude of first arrivals of the observed and synthetic seismograms shown in Fig. S7. A sub-OAML low velocity volume that is at least 2 km thick produces attenuation in near-ridge seismograms (~20 km offset) of 1.8 natural log units (100-m-thick OAML, top) and 2.0 log units (50-m-thick OAML, bottom), comparable to the 1.9 ± 0.5 natural log units decrease in RMS amplitude observed in ORB-05 data (Fig. 4c).

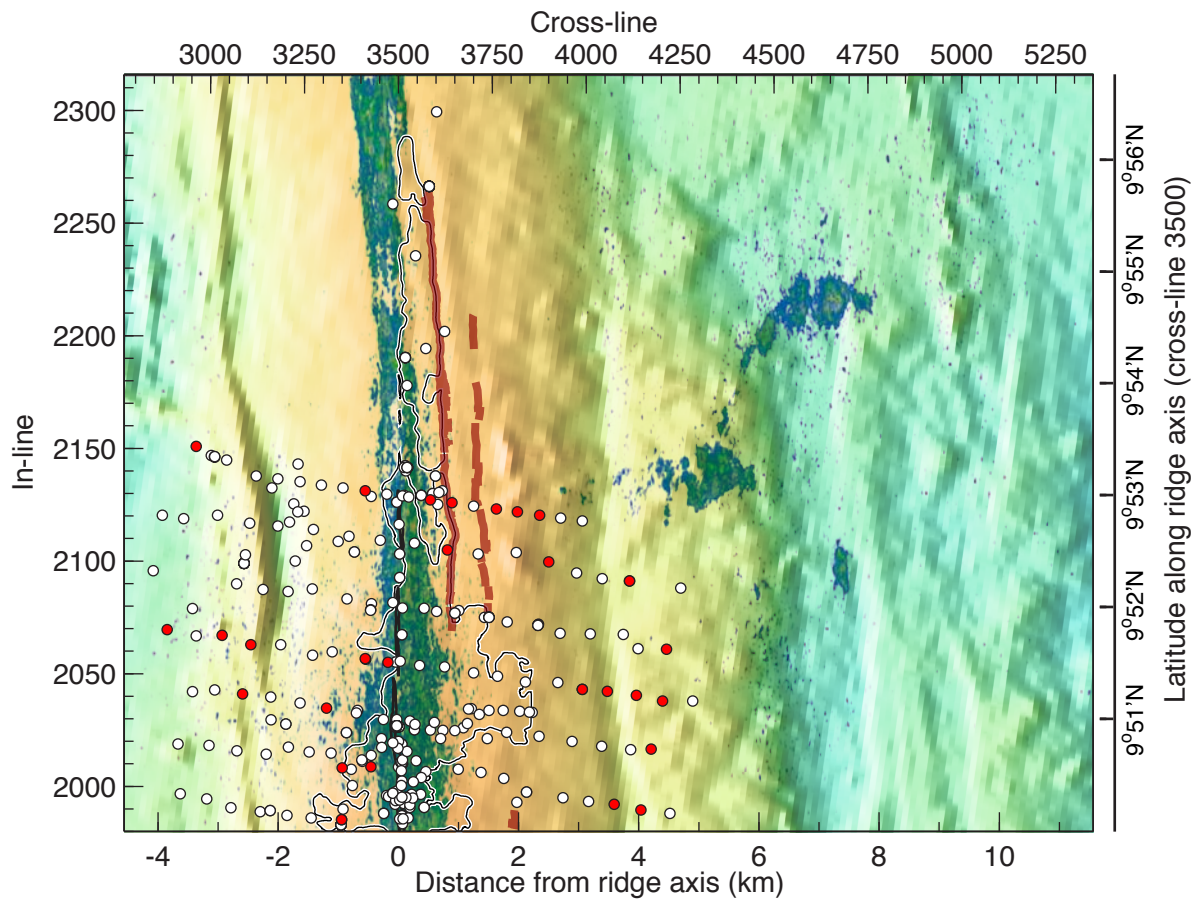


Figure S9. Seismic reflection energy projected over seafloor bathymetry as in Fig. 2b. Circles correspond to locations of existing lava samples that have been analyzed for major element composition (TiO_2 and K_2O). Red and white symbols correspond to enriched and normal compositions, respectively. Enriched composition is defined as $\text{wt \% K}_2\text{O}/\text{TiO}_2 > 0.1$. Data are from the Petrological Database of the Ocean Floor (<http://www.petdb.org>).